Volume 23
Number 40
28 October 2021
Pages 22819–23392

PCCP

Physical Chemistry Chemical Physics

rsc.li/pccp

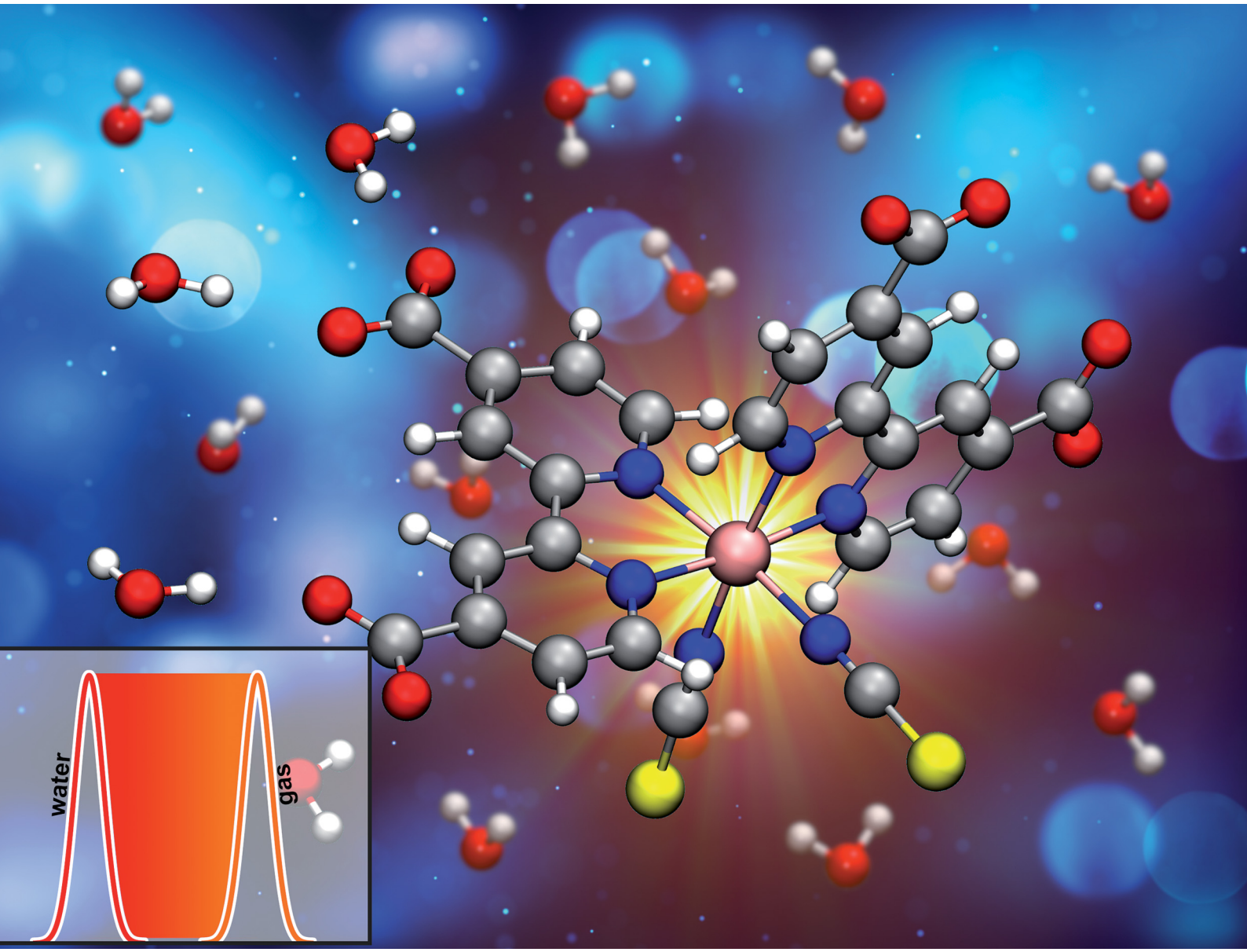

ISSN 1463-9076

ROYAL SOCIETY OF CHEMISTRY

PAPER

Alessio Petrone, Nadia Rega *et al.*
Direct observation of the solvent organization and nuclear vibrations of $[Ru(dcbpy)_2(NCS)_2]^{4-}$, [dcbpy = (4,4′-dicarboxy-2,2′-bipyridine)], *via ab initio* molecular dynamics

PCCP

ROYAL SOCIETY OF CHEMISTRY

PAPER

View Article Online
View Journal | View Issue

Check for updates

Cite this: *Phys. Chem. Chem. Phys.*, 2021, **23**, 22885

Direct observation of the solvent organization and nuclear vibrations of $[Ru(dcbpy)_2(NCS)_2]^{4-}$, [dcbpy = (4,4′-dicarboxy-2,2′-bipyridine)], *via ab initio* molecular dynamics†

Fulvio Perrella,[a] Alessio Petrone *[ab] and Nadia Rega *[abc]

Environmental effects can drastically influence the optical properties and photoreactivity of molecules, particularly in the presence of polar and/or protic solvents. In this work we investigate a negatively charged Ru(II) complex, $[Ru(dcbpy)_2(NCS)_2]^{4-}$ [dcbpy = (4,4′-dicarboxy-2,2′-bipyridine)], in water solution, since this system belongs to a broader class of transition-metal compounds undergoing upon photo-excitation rapid and complex charge transfer (CT) dynamics, which can be dictated by structural rearrangement and solvent environment. *Ab initio* molecular dynamics (AIMD) relying on a hybrid quantum/molecular mechanics scheme is used to probe the equilibrium microsolvation around the metal complex in terms of radial distribution functions of the main solvation sites and solvent effects on the overall equilibrium structure. Then, using our AIMD-based generalized normal mode approach, we investigate how the ligand vibrational spectroscopic features are affected by water solvation, also contributing to the interpretation of experimental Infra-Red spectra. Two solvation sites are found for the ligands: the sulfur and the oxygen sites can interact on average with ∼4 and ∼3 water molecules, respectively, where a stronger interaction of the oxygen sites is highlighted. On average an overall dynamic distortion of the C_2 symmetric gas-phase structure was found to be induced by water solvation. Vibrational analysis reproduced experimental values for ligand symmetric and asymmetric stretchings, linking the observed shifts with respect to the gas-phase to a complex solvent distribution around the system. This is the groundwork for future excited-state nuclear and electronic dynamics to monitor non-equilibrium processes of CT excitation in complex environments, such as exciton migration in photovoltaic technologies.

Received 11th July 2021,
Accepted 11th August 2021

DOI: 10.1039/d1cp03151a

rsc.li/pccp

Published on 11 agosto 2021. Downloaded on 28/08/2024 14:03:37.

1 Introduction

The Ru(II) complex $[Ru(dcbpy)_2(NCS)_2]^{4-}$, [dcbpy = (4,4′-dicarboxy-2,2′-bipyridine)] (Fig. 1) or "$N3^{4-}$" is a popular and efficient dye, employed in solar cell and light harvesting applications.[1–9] N3 and its charged variants belong to a broader class of transition-metal compounds undergoing rapid and complex photo-induced charge transfer (CT) dynamics, which can be dictated by structural and solvent rearrangements. Such CT dynamics can involve multiple electronic states from the singlet initial metal to ligand charge transfer ^{1}MLCT photo-induced state(s). Then, an ultrafast inter-system crossing (ISC) leads to a long-lived final triplet ^{3}MLCT, both in solution[10–15] and on semiconductor substrates.[16–23] New insights about the fast N3 ISC have been recently offered by 2D electronic-vibrational spectroscopy in water solution.[24] ^{1}MLCT states that are vibronically coupled to ^{3}MLCT vibrational modes and so likely involved in the ISC were in fact identified. Such states, called $^1MLCT_A$ and $^1MLCT_B$, respectively located at 24 400–24 700 cm^{-1} (410–405 nm) and 25 000–25 300 cm^{-1} (400–395 nm), are characterized by an important electronic density redistribution from the $Ru(NCS)_2$ moiety towards the dcbpy rings, with a transition electric dipole moment predominantly located on the equatorial plane.[25,26] Vibrational modes involving both the $Ru(NCS)_2$ charge-donor and the dcbpy charge-acceptor segments on the $N3^{4-}$ molecule are then probed with a mid-IR pulse to correlate as many ^{1}MLCT states as possible with the final ^{3}MLCT. The electron density on the dcbpy ligands should affect the carboxylate vibrations, because an increased electron density is expected to downshift the vibrational frequency.

[a] *Department of Chemical Sciences, University of Napoli Federico II, Complesso Universitario di M.S. Angelo, via Cintia 21, I-80126, Napoli, Italy. E-mail: alessio.petrone@unina.it, nadia.rega@unina.it*
[b] *Scuola Superiore Meridionale, Largo San Marcellino 10, I-80138, Napoli, Italy*
[c] *CRIB, Centro Interdipartimentale di Ricerca sui Biomateriali, Piazzale Tecchio 80, I-80125, Napoli, Italy*

† Electronic supplementary information (ESI) available: Graphical representation of the spherical water box, Mulliken population analysis on 10wat/CPCM cluster, the optimized 10wat/CPCM cluster and solvation sites for the $N3^{4-}$ system, X–O(wat) RDF plot along with maxima r_{max} values and the corresponding integrated number of solvent molecules in the first shell for each $N3^{4-}$ solvation site, reduced $N3^{4-}$ model for C_2 continuous symmetry measure (CSM) calculations. See DOI: 10.1039/d1cp03151a

Published on 11 agosto 2021. Downloaded on 28/08/2024 14:03:37.

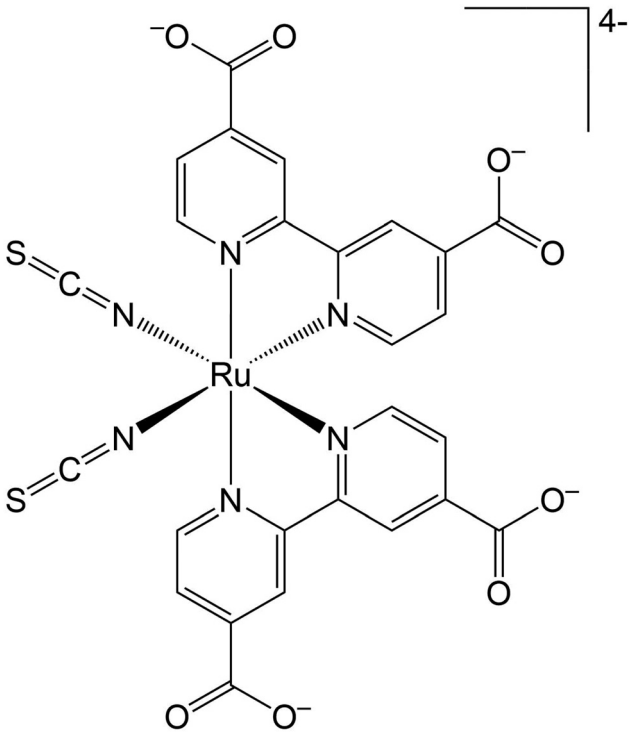

Fig. 1 $[Ru(dcbpy)_2(NCS)_2]^{4-}$, [dcbpy = (4,4′-dicarboxy-2,2′-bipyridine)] '$N3^{4-}$' Ru(II) complex.

The carboxylate IR bands and their anisotropic transient absorption should therefore be good reporters on the localization of the MLCT excitation. Moreover, these carboxylate vibrational bands are quite sensitive to the adsorption modes of $N3^{4-}$ onto TiO_2, since the carboxylates act as anchoring groups on the semiconductor surface.[8,27] In addition, time-resolved IR measurements on PbS colloidal quantum dots were used to distinguish intraband *vs.* trap-to-band transitions based on the presence of ligand carboxylate stretching vibrational signatures.[28–30]

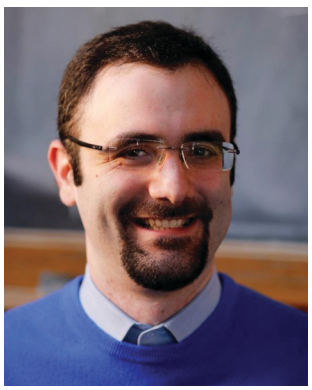

Alessio Petrone

Alessio Petrone received his PhD in Chemical Sciences at University of Napoli Federico II (Italy) in 2014. Then, he spent almost 5 years as Research Associate in the U.S. working at University of Washington (Seattle, USA), being also part of the US national center of excellence University of Washington Molecular Engineering Materials Center. Since 2019, He is Assistant Professor (RTD-A) at University of Napoli Federico II in Napoli (Italy) in the Department of Chemical Sciences. His research focuses on the theoretical modeling of non-equilibrium processes of photo-generated species and on developing ab initio molecular dynamics techniques for time resolved spectroscopies. Photo Credit: Dr. Shichao Sun.

Environmental effects can drastically influence the optical properties and photoreactivity of molecules, particularly in the presence of polar and/or protic solvents.[31–40] Exactly knowing the equilibrium solvation of a CT system in solution, such as $N3^{4-}$, is crucial since, for example, the atomistic interpretation of time-resolved signals and non-equilibrium CT dynamics can be derived from photoinduced changes of hydrogen bonding between the solute and nearby water molecules.[41,42] Discriminating the solvent effects from the charge recombination is the first step of our study of $N3^{4-}$ system, because the metal–ligand complex wave function is influenced by ligand-solvent binding and the high-frequency vibrational modes of the ligands are also expected to play a role in the exciton dynamics.[43]

From a theoretical and computational perspective, accurately simulating and modeling the solute–solvent interactions is very challenging, but at same time mandatory to provide a molecular picture of the interplay between spectroscopic data and microsolvation. Once solvent effects and charge redistribution upon excitation combine together, theory is required to disentangle these effects on both the (non) equilibrium microsolvation and the vibration dynamics of photoactive molecules in solution. Routinely used computational spectroscopy relies on the study of solute–solvent clusters corresponding to energy minimum structures on the potential energy surface that are representative, on average, of the dye microsolvation. As a complementary approach, configurational sampling provided by *ab initio* molecular dynamics (AIMD) simulations may be a suitable choice to describe solvent effects on solute chemical-physical properties and spectroscopic features. Describing the solvent by a flexible model, as in this work, is also required for this aim to provide a more accurate description of solute–solvent dynamics, in particular those of possible hydrogen-bond networks, strongly impacting several system properties, that is, solvent viscosity, mobility of solvation shells, solute–solvent vibrational couplings.

Solute–solvent vibrations and electrostatic interactions with bulk solvent are indeed the main actors in predicting accurate Infrared and Raman vibrational spectra. Nowadays, different protocols exist to also enable the vibrational analysis using these AIMD-based methods, expressing the *ab initio* molecular dynamics in normal-like modes. These modes, hereafter called generalized modes, correspond to vibrational frequencies that are anharmonic and coupled in nature.[44–46] In this work, we employed *ab initio* molecular dynamics relying on a hybrid quantum/molecular mechanic (QM/MM) scheme to probe the equilibrium microsolvation around $N3^{4-}$ in terms of radial distribution functions of the main solvation sites along with monitoring the effects of solvent on the overall equilibrium structure. Then, using the AIMD-based generalized normal mode approach, we investigate how $N3^{4-}$ vibrational spectroscopic features are affected by water solvation, also contributing to the interpretation of experimental Infra-Red(IR) spectra. Density functional theory (DFT) was employed for the *ab initio* treatment of the QM part, since it has an optimal balance between accuracy and computational cost and, in its hybrid version, it has been vastly used for the theoretical

 This journal is © the Owner Societies 2021

Published on 11 agosto 2021. Downloaded on 28/08/2024 14:03:37.

characterization of both vibrational/dynamical properties of molecules[47–49] and the description of the electronic structure of both the ground and excited electronic states in macro-molecular systems of material[50–62] or biological[63–71] interest. Moreover, DFT and its time-dependent version have shown to be effective for theoretical characterization of many Ru complexes in different environments.[72–89] This study represents an important starting point for future excited-state nuclear and electronic dynamics to gauge non-equilibrium processes of CT excitation in complex environments, such as exciton migration in photovoltaic technologies.

2 Methods

2.1 Computational details

A ground-state molecular dynamics trajectory of $N3^{4-}$ compound in explicit water solution was collected. A spherical box (of 22 Å radius, Fig. S1, ESI†) including explicitly at least four solvation shells for each $N3^{4-}$ site was carved out from a previously equilibrated larger cubic box (extracted from the AmberTools[90] solvent box database) whose density resembled the experimental value at 298 K. The $N3^{4-}$, treated at DFT level, was then located at the center of the resulting sphere (eliminating the colliding water molecules in the same region), retaining a final number of 1462 water molecules, treated at MM level and described by the TIP3P force field.[91] In particular, a flexible version of the TIP3P water model was employed, which includes the water bending contribution.[92] A parametrization procedure gave as water bending force field parameters θ_0 = 104.52°, k_θ = 50 kJ mol^{-1} rad^{-2}. A flexible MM solvent model has proven in fact useful to accurately describe coupled solute–solvent motions.[92] The electronic structures of QM part were obtained by solving the Kohn–Sham equation using the global hybrid Becke, 3-parameter, Lee–Yang–Parr (B3LYP) density functional[93–95] with the def2-SVP[96] basis set and associated electronic core potential (ECP) for Ru.[97] This level of theory was already validated in a previous study for the system under investigation.[98] The QM and MM potentials were combined according to the ONIOM QM/MM scheme.[99–102] The electrostatic interaction between QM and MM layers was treated including the MM charges in the QM Hamiltonian (*i.e.*, an 'electronic' embedding). General AMBER Force Field[103] atom types (and so van der Waals non-bonding parameters) were assigned to the $N3^{4-}$ atoms.

Non-periodic boundary conditions were introduced through a hybrid explicit/implicit solvent model.[67,104–107] A solute–solvent explicit (*i.e.*, atomistic) system is confined in a fixed-radius sphere and perturbed by the mean field of the surrounding bulk, implicit, solvent. The explicit part can be so considered as an *NVT* ensemble. The Helmholtz free energy (A) for a given nuclear configuration $\boldsymbol{R}$ and electronic density $\boldsymbol{P}$ of the explicit system can be derived as:

$$A(\boldsymbol{R}) = E(\boldsymbol{R},\boldsymbol{P}) + W(\boldsymbol{R},\boldsymbol{P}) \quad (1)$$

being $E(\boldsymbol{R},\boldsymbol{P})$ and $W(\boldsymbol{R},\boldsymbol{P})$ the internal energy (obtained at an *ab initio* level) and the solvent mean field contribution, respectively. W can be considered as the work needed to charge interactions between the explicit and the implicit systems and it can be decomposed as:

$$W(\boldsymbol{R}) = W_{\text{disp-rep}}(\boldsymbol{R}) + W_{\text{elec}}(\boldsymbol{R}) + W_{\text{cav}}(\boldsymbol{R}) \quad (2)$$

W_{cav} (the cavitation free energy) is constant for an *NVT* model and so not explicitly included. W_{elec} accounts for the long-range electrostatic interactions between the explicit solute–solvent subsystem and the bulk solvent. It can be included through a self-consistent reaction field method, such as the Polarizable Continuum Model (PCM)[108–110] in its conductor-like version.[111–115] $W_{\text{disp-rep}}$ accounts instead for the contribution of the short-range dispersion-repulsion interactions between the explicit system and the outer bulk solvent. This term is modeled by an empirical potential. The $W_{\text{disp-rep}}(\boldsymbol{R})$ potential, actually a radial function $W_{\text{disp-rep}}(r)$ acting on the center of mass of the explicit solvent molecules, provides effective non-periodic boundary conditions and it depends on the solvent density, the temperature and the chosen solvent molecular model.[116] The procedure combining nonPBC and QM/MM AIMD was originally presented in ref. 104.

A preliminary equilibration step of ~2 ps was carried out on our system, then a ~8.6 ps production run was collected. A T = 298 K temperature was kept during the production through velocity rescaling every 1 ps. The Atom-centered Density Matrix Propagation extended Lagrangian approach (ADMP) was employed:[117–119] the density matrix in an orthonormal Gaussian atom-centered basis is propagated along with the nuclear degrees of freedom, avoiding a convergence procedure at each step. A mass-weighting scheme which attributes a higher mass to the core functions was chosen, together with a 0.2 amu bohr^2 valence mass. This allowed to employ a 0.1 fs time step, obtaining a total energy conservation within 0.01 hartree.

Concerning static calculations, two representative $N3^{4-}$ geometries were obtained *via* energy minimization procedure either in gas-phase or using a $N3^{4-}$ plus explicit water molecules cluster model embedded in implicit solvent (in its conductor-like version). One solvent molecule was added for each solvation site (Fig. S2, ESI,† namely 10wat/CPCM).

Table 1 Mean (st.dev.) selected $N3^{4-}$ structural parameters from *ab initio* molecular dynamics (AIMD) in explicit water solution. Values from $N3^{4-}$ in either gas-phase or plus explicit water molecules cluster model embedded in implicit solvent (10wat/CPCM) are also given for comparison. For the gas-phase and cluster models a single value is reported since they are identical

	AIMD	Gas-phase	10wat/CPCM
Ru–N_{ax}(dcbpy)	2.10 (0.05) 2.09 (0.05)	2.091	2.085
Ru–N_{eq}(dcbpy)	2.08 (0.05) 2.08 (0.05)	2.086	2.071
Ru–N(NCS)	2.06 (0.06) 2.07 (0.06)	2.067	2.054
N_{ax}(dcbpy1)–Ru–N_{eq}(dcbpy2)	100 (4) 97 (3)	98.08	97.25
N(NCS1)–Ru–N(NCS2)	89 (4)	89.82	90.40
Ru–N(NCS)–C(NCS)	165 (7) 165 (7)	177.20	177.94

Published on 11 agosto 2021. Downloaded on 28/08/2024 14:03:37.

Geometries were considered fully optimized when both the forces (maximum and RMS force, 0.000450 and 0.000300 hartree $bohr^{-1}$ thresholds, respectively) and displacement (maximum and RMS displacement, 0.0018 and 0.0012 bohr thresholds, respectively) values for all atoms were below the threshold criteria.

In all calculations the part treated at DFT level was assumed to have an overall 4− charge. We checked that in the ground state the entire negative charge was mostly located on the $N3^{4-}$ by performing Mulliken population analysis on the 10wat/CPCM cluster, where in principle the 10 closest water molecules can partially accept the negative charge. In fact, a $-3.77\ e^-$ charge (94.32%) is actually located on the $N3^{4-}$, while only a $-0.23\ e^-$ charge (5.68%) is overall found on the first-shell solvent molecules, meaning that each water molecule presents a very small amount of charge on average ($\sim -0.02\ e^-$, please refer to

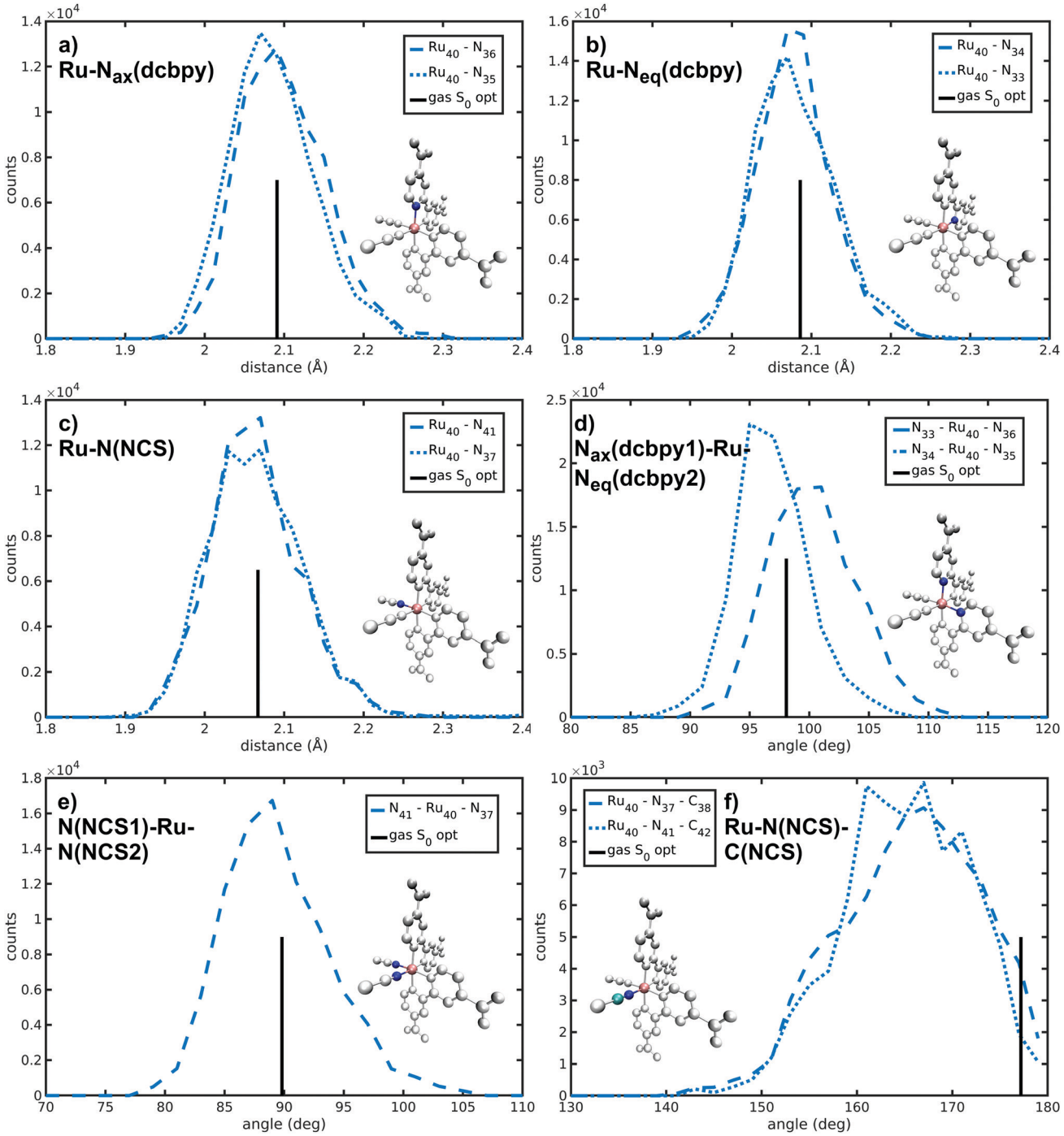

Fig. 2 Distributions of selected $N3^{4-}$ structural parameters from an *ab initio* Molecular Dynamics simulation in explicit water solution. Values observed in the gas-phase optimized structure are also shown as vertical black bars with arbitrary height.

 This journal is © the Owner Societies 2021

Published on 11 agosto 2021. Downloaded on 28/08/2024 14:03:37.

Table S1 in the ESI† for the atomic charges and the total charges on $N3^{4-}$ and 10 water molecules).

All calculations were performed with a development version of the Gaussian software.[120]

2.2 Vibrational analysis

Besides routine normal mode vibrational analysis through diagonalization of the Hessian matrix evaluated at an energy minimum structure, generalized, anharmonic, modes at finite temperature can be extracted from a Molecular Dynamics phase-space sampling.[44,45,121,122]

In the following discussion, the cartesian atomic coordinates and generalized normal modes coordinates are respectively called $\boldsymbol{q}(t) = \{q_i(t)\}$ and $\boldsymbol{Q}(t) = \{Q_k(t)\}$. The generalized normal modes are defined such that the velocities $\dot{Q}_k$ are non-correlated:

$$\langle \dot{Q}_k(t)\dot{Q}_l(t)\rangle \approx \delta_{kl} \quad (3)$$

where δ_{kl} is the Kronecker delta and $\langle\cdot\rangle$ denotes an ensemble average, constructed in this work by averaging over time the required quantities over a single collected trajectory.

Generalized normal modes (GNMs) directions are obtained as the eigenvectors of the covariance matrix $\boldsymbol{K}$ of the atomic mass-weighted velocities:

$$K_{ij} = \frac{1}{2}(m_i m_j)^{1/2}\langle(\dot{q}_i - \langle\dot{q}_i\rangle)(\dot{q}_j - \langle\dot{q}_j\rangle)\rangle \quad (4)$$

where m_i is the mass associated to the coordinate q_i and $\dot{q}_i$ is q_i velocity.

Generalized modes velocities are calculated as the projections of atomic velocities along the generalized normal modes directions:

$$\dot{\boldsymbol{Q}}(t) = \boldsymbol{L}^{\dagger}\dot{\boldsymbol{q}}(t) \quad (5)$$

where $\boldsymbol{L}$ is the matrix that diagonalizes $\boldsymbol{K}$ (*i.e.*, the eigenvectors matrix) and $\dot{\boldsymbol{q}}$ is the atomic velocity vector.

The frequency associated with the k-th generalized mode can be then obtained by the Fourier Transform of the mode velocity $\dot{Q}_k$ autocorrelation (*i.e.*, $\dot{Q}_k$ power spectrum):

$$P_k(\nu) = \int\langle\dot{Q}_k(\tau)\dot{Q}_k(\tau+t)\rangle_\tau e^{-i\omega t}dt = \left|\int\dot{Q}_k(t)e^{-i\omega t}dt\right|^2 \quad (6)$$

In order to observe only $N3^{4-}$ internal motions and to exclude rotational contributions, a minimization procedure of the angular momentum was performed, based upon the rotation of the structure at each trajectory step onto the starting orientation. In particular, specific angular momentum minimizations were applied in $N3^{4-}$ carboxylate and thiocyanate vibrational analyses. In the former, the rotation aimed at superimposing the carboxylate groups and the linked pyridine rings on the first frame, while in the latter, the thiocyanate ligands and the Ru atom were superimposed. The vibrational analysis was performed on only the $N3^{4-}$ solute velocities in order to extract its generalized normal modes. Nevertheless, solvent effects contribute to such modes, since the $N3^{4-}$ dynamics was collected in explicit solvent.

3 Results and discussion

3.1 $N3^{4-}$ structure and solvation in water solution

$N3^{4-}$ main coordination structural parameters sampled by *ab initio* MD in explicit water solution have been compared to those of two representative structures obtained *via* energy minimization procedure by adopting the same level of theory (see Methods section). We wish to point out that AIMD provide not only average values, but also their equilibrium distributions. The Ru-ligand distances in water solution are totally comparable to those obtained from both optimized structures, differing at most for 0.01 Å (Table 1 and Fig. 2a–c). In particular, the Ru–N(dcbpy) bonds (2.08 Å for the equatorial bonds, 2.09–2.10 Å for the axial ones) are only 0.01–0.04 Å longer than the Ru–N(NCS) bonds. The two N_{ax}–Ru–N_{eq} angles involving different dcbpy ligands (so not being the dcbpy N–Ru–N bite angle and not being constrained by dcbpy chelation), as well as the NCS–Ru–NCS angle, seem not to be affected by water solvation (Fig. 2d and e). While the former assume a $\approx 100^\circ$ value, the latter retains an almost ideal octahedral (89°) angle. A solvation-induced distortion can be observed instead in the Ru–N(NCS)-C(NCS) angles, describing isothiocyanate coordination linearity. While in both optimized (gas-phase and 10wat/CPCM) structures NCS^- coordination is actually almost linear ($\approx 177^\circ$), the AIMD trajectory in explicit water solution samples, on average, a slightly bent coordination (165°, Fig. 2f), showing

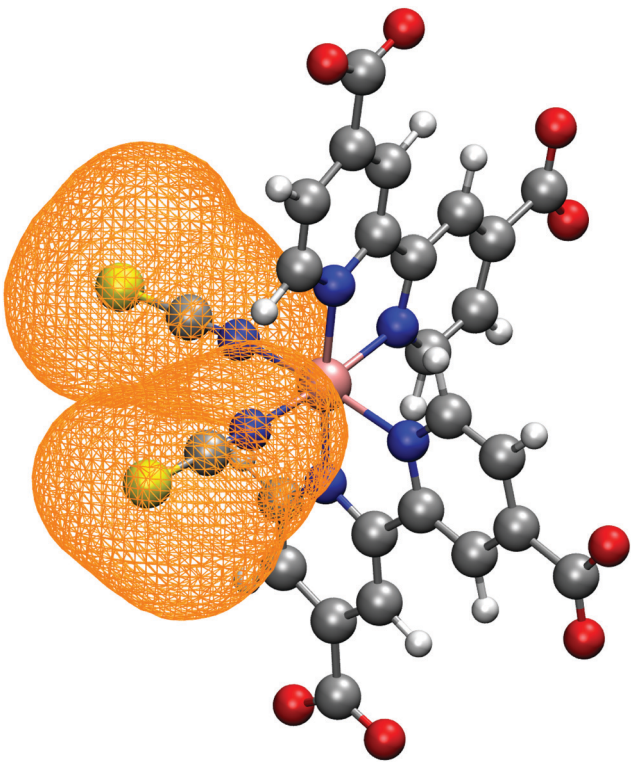

Fig. 3 NCS^- ligands spatial distribution, calculated as trajectory-averaged occupancy map with the *volmap* tool of VMD program.[123] The map isosurface (0.2 isovalue) is depicted as orange wireframe around the ligands.

Published on 11 agosto 2021. Downloaded on 28/08/2024 14:03:37.

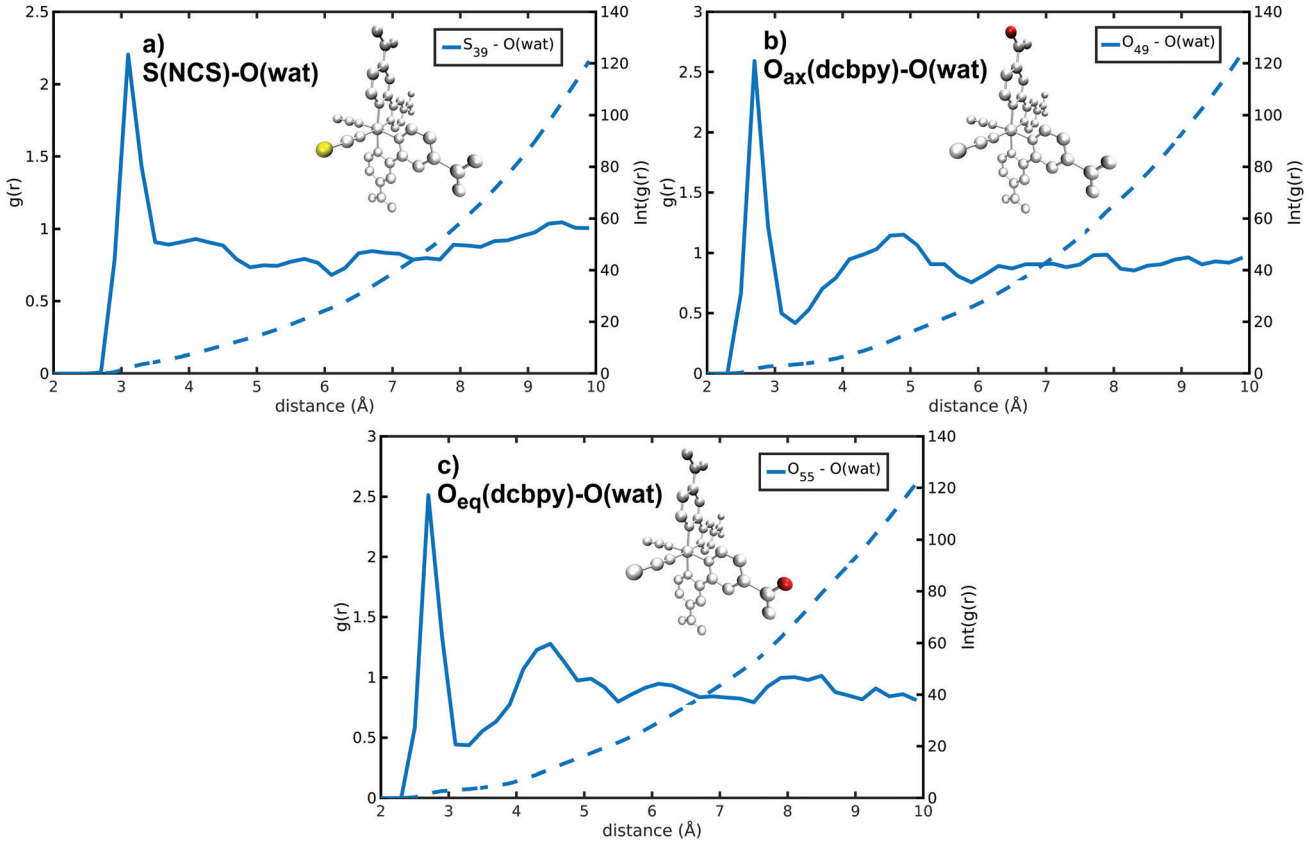

Fig. 4 S(NCS)–O(wat) and O(dcbpy)–O(wat) radial distribution functions and integrated number of solvent molecules for selected S(NCS$^-$) and O(dcbpy) N3^{4-} solvation sites.

moreover some conformational flexibility ($\approx 7^\circ$ standard deviation). A trajectory-averaged isodensity plot of the occupancy map of NCS moieties reveals in fact a conic-shaped region actually explored by NCS$^-$ ligands (Fig. 3).

N3^{4-} microsolvation in water solution has been investigated in detail next. The N3^{4-} complex has in fact several solvation sites on NCS$^-$ sulfur and dcbpy oxygen atoms (Fig. S3, ESI†), both able to interact with the surrounding solvent molecules. Because of N3^{4-} high negative charge, a strong solvation by polar solvents (such as water) is expected. Solute–solvent $g(r)$ radial distribution functions reveal that the water molecules are mostly found at 3.10 and 2.70 Å from S(NCS$^-$) and O(dcbpy), respectively (S(NCS)–O(wat) and O(dcbpy)–O(wat) $g(r)$ peaks, Fig. 4 and Fig. S4 and Table 2 and Table S2, ESI†). The solvent molecules are therefore closer to the oxygen sites, likely because of the dcbpy oxygen atoms higher negative charge and smaller atomic radius. However, sulfur atoms can interact on average with a number (~ 4) of water molecules higher than oxygen sites (~ 3). Looking in detail at S–O(wat) and O–O(wat) $g(r)$ features, actually the sulfur solvation peaks do not appear much less structured than the oxygen ones. Nevertheless, a second solvation shell at a 4.5–5 Å distance can be observed only for the oxygen sites.

Table 2 Average S(NCS)–O(wat) and O(dcbpy)–O(wat) radial distributions maxima r_{max} and integrated number of solvent molecules in the first shell n_{wat}

	r_{max} (Å)	n_{wat}
S(NCS)	3.10	4.44
O(dcbpy)	2.70	3.31

Finally we monitored the probability of finding water molecules around the solvation sites. For this purpose, isodensity plots of spatial distributions of water molecules around O(dcbpy) and S(NCS) are reported in Fig. 5. Comparing the two distributions at the same occupancy isovalue (0.3) and within the same distance (3.5 Å) from the O(dcbpy) and S(NCS) sites, some differences can be observed. In fact, while solvent occupancy is slightly higher and more uniform around dcbpy carboxylate groups (Fig. 5a), a more diffuse and less tight distribution around NCS$^-$ ligands can be instead observed (Fig. 5b).

Monitoring the ground-state finite temperature N3^{4-} microsolvation *via* the average number of water interactions, their distances and their spatial distribution around the solvation sites is a very important information, since the changes in these parameters are proxy of CT dynamics and can be probed by frequency shifts in time-resolved spectroscopic signals.

The dynamical perturbation of N3^{4-} structural symmetry in water solution is then explored. N3^{4-} "ideal" minimum energy

 This journal is © the Owner Societies 2021

Published on 11 agosto 2021. Downloaded on 28/08/2024 14:03:37.

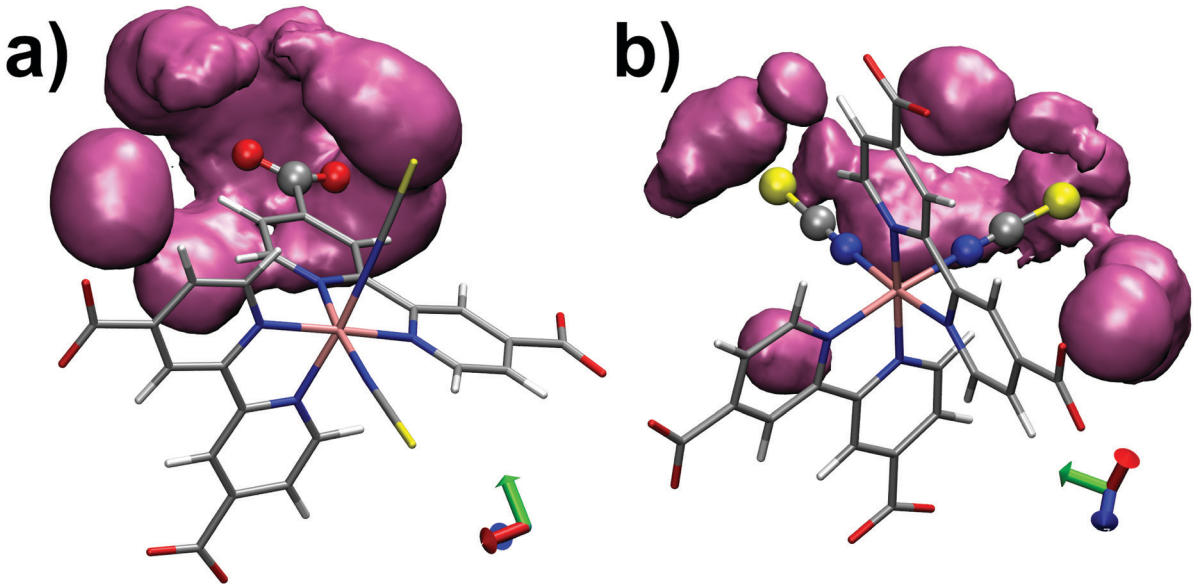

Fig. 5 Isodensity plots (0.3 occupancy isovalue) of water molecules spatial distributions around O(dcbpy) (a) and S(NCS) (b) within 3.5 Å, calculated as trajectory-averaged O(wat) occupancy maps with the *volmap* tool of VMD program.[123]

geometry belongs in fact to the C_2 symmetry group, with its C_2 symmetry axis bisecting the NCS–Ru–NCS angle (please refer to Fig. 1). Nevertheless, vibration and environment effects are indeed able to instantaneously lower such symmetry to some degree. This dynamic deviation from a symmetric structure is relevant first from a spectroscopic point of view, since it provides a mechanism to overcome in part symmetry-based selection rules. The transition probability of dark electronic states, forbidden in an ideal, "frozen", geometry, could therefore increase. Moreover, in the specific case of N3 and other Ru-polypyridyl complexes, the localized nature of MLCT excited states, with the photo-excited electron on only one bipyridine ligand, has been recognized as a result of symmetry-breaking vibrations and environment fluctuations.[7,124–133] The localization of CT excitation is potentially relevant, since it enables intra-molecular, inter-ligand electron transfer processes among bpy acceptor ligands.[131–133]

A continuous symmetry measure (CSM) of $N3^{4-}$ minimal deviation from C_2 symmetry (*i.e.*, the minimized root mean square (r.m.s.) deviation of the structure from its image generated through the C_2 operation, normalized to the r.m.s. size of the structure)[134–136] has been evaluated along the AIMD trajectory in water solution. To improve computational efficiency, a reduced $N3^{4-}$ model (a smaller model able to retain a symmetry not higher than C_2 as the full $N3^{4-}$ structure, Fig. S5, ESI†) has been employed for C_2-CSM calculations. Looking at the distribution from the $N3^{4-}$ AIMD in water solution (Fig. 6), two small CSM values ($\sim$0.1 and 0.2) appear as the most populated, although higher symmetry distortions ($\sim$0.45) are occasionally also explored. Therefore, compared to the static minimum energy structure having an ideal C_2 symmetry (zero CSM value), the dynamical picture offered by AIMD simulations reveals that $N3^{4-}$ at room temperature in water solution actually slightly

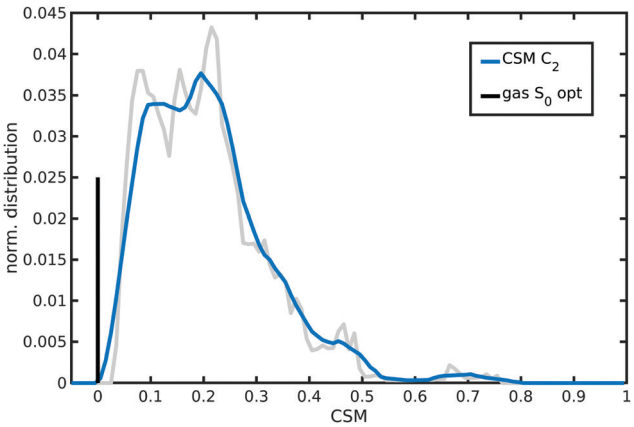

Fig. 6 Normalized distribution of the continuous symmetry measure (CSM) with respect to C_2 symmetry group sampled by $N3^{4-}$ AIMD in water solution. CSM values have been calculated with the program provided in ref. 136. A lower value in the [0,1] range corresponds to a more symmetric structure. An averaged distribution function (the blue curve) is shown for better clarity. The zero value of the optimized gas-phase $N3^{4-}$ symmetric structure is also reported as a vertical black bar with arbitrary height.

Table 3 Selected $N3^{4-}$ vibrational frequencies obtained through static harmonic and dynamical vibrational analysis. If available, also experimental, water solution, values[24] are reported for comparison

		Static, harmonic		
	Experimental	Gas-phase	10wat/CPCM	AIMD
ν_{symm}(COO) (cm^{-1})	1375	1368	1409	1354
ν_{asymm}(COO)	1596	1767	1700	1621
ν(CN)	2120	2210	2209	2080
ν(CS)		820	814	786

Published on 11 agosto 2021. Downloaded on 28/08/2024 14:03:37.

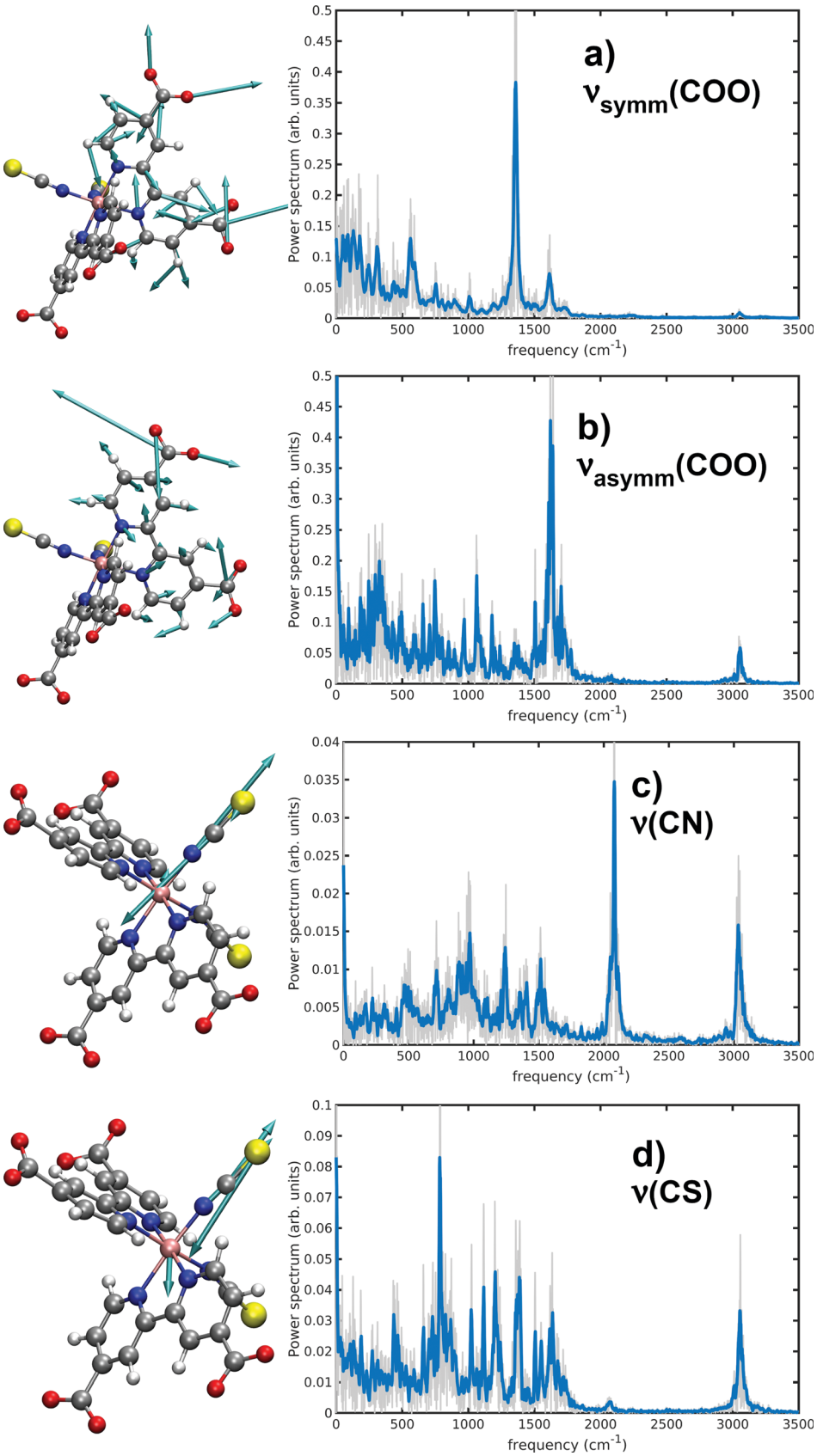

Fig. 7 Selected generalized modes from $N3^{4-}$ dynamical vibrational analysis. Graphical representations of generalized modes directions are reported in left panels; only the vectors on a single ligand are depicted for better clarity. Generalized modes power spectra are displayed on right panels.

 This journal is © the Owner Societies 2021

Published on 11 agosto 2021. Downloaded on 28/08/2024 14:03:37.

deviates, on average, from the C_2 symmetry, due to its vibrational motions and solvent environment fluctuations (mean C_2-CSM: 0.21 ± 0.12). Such $N3^{4-}$ symmetry-lowering flexibility can potentially make dark excited states experimentally accessible and contributes to localize the photo-excited electron in MLCT states.

3.2 $N3^{4-}$ vibrational signatures

Several works have experimentally characterized the $N3^{4-}$ IR absorption, in solution,[24,131] in the solid state and adsorbed onto TiO_2 films.[8,27] Experimental frequencies from ref. 24 are here provided for comparison, since they were measured in water solution as our calculated ones. As already discussed in Methods section, a vibrational analysis of the sampled $N3^{4-}$ AIMD trajectory in water solution necessarily includes both anharmonicity and solvent effects, which cannot be completely captured instead by 'static' vibrational calculations (*i.e.*, evaluating the Hessian matrix on a minimum energy structure). In particular, dcbpy carboxyl groups symmetric and asymmetric stretchings and thiocyanates C═N and C═S stretching modes have been characterized through both approaches (Table 3 and Fig. 7). Two static vibrational calculations have been performed for comparison, one on the gas-phase optimized $N3^{4-}$ structure and another on the optimized 10wat/CPCM cluster (Fig. S2, ESI†).

From the displacement vectors of generalized modes it can be seen that *ab initio* MD-based vibrational analysis can be used to catch the nature of the system normal modes. Considering first the symmetric COO^- stretching (experimentally found at 1375 cm^{-1}), the inclusion of solvent effects through the two distinct approaches (explicitly adding some QM water molecules and introducing an implicit bulk solvent, or a dynamics in explicit MM water) leads to opposite deviations from the harmonic gas-phase value (10wat/CPCM: 41 cm^{-1}, AIMD: -14 cm^{-1}, respectively). The 'dynamical' approach results to be more accurate with a -21 cm^{-1} error, if both approaches are compared to the experiment. Both solvent methods predict instead a red-shift of the asymmetric COO^- stretching (experimentally at 1596 cm^{-1}) from the gas-phase harmonic value (10wat/CPCM: -67 cm^{-1}, AIMD: -146 cm^{-1}); the higher red-shift by the AIMD vibrational approach allows again a lower (25 cm^{-1}) error *vs.* the experimental value. This important red shift has been previously noted to be typical of carbonyl moieties of amidic groups in aqueous solution as well.[92] This is due to the weakening of the double bond nature of the CO bond because of the oxygen interaction with surrounding water molecules. Monitoring their dynamical evolution over time can be used to show the intrinsic dynamical nature of the system also under equilibrium conditions. As matter of fact, all AIMD spectra are enriched indeed with low frequency bands related to the coupling with water librations and collective hydrogen bond stretching and bending (region of 100–400 cm^{-1}) modes.

While the inclusion of one explicit QM water molecule near each NCS^- ligand does not significantly alter the gas-phase C═N and C═S stretchings, the AIMD vibrational analysis reveals instead red-shifts of -130 and -34 cm^{-1}, achieving a better accuracy in particular for the C═N stretching (a -40 cm^{-1} error from the 2120 cm^{-1} experimental value).

4 Conclusions

Our work provides an investigation of equilibrium solvation of $N3^{4-}$ in water, where the metal–ligand–water structuration and equilibrium fluctuations are investigated in details *via ab initio* molecular dynamics. Two solvation sites are found for the ligands: the sulfur and the oxygen sites can interact on average with $\sim$4 and $\sim$3 water molecules, respectively. A stronger interaction of the oxygen sites (RDF maximum at 2.70 Å) with respect to the sulfur ones (RDF maximum at 3.10 Å) is highlighted by this study. Additionally we find that a dynamic distortion of the C_2 symmetric structure, revealed by a continuous symmetry measure, is induced by molecular internal motions and water solvation, mostly modifying the NCS^- ligand coordination geometry, which is influenced by a precession motion, as clearly identified by isodensity maps.

Analyzing solute–solvent hydrogen bonding network is very important for monitoring the CT dynamics of these systems since the strong modification of the solvent network induced by electronic excitation of the solute can provide useful molecular insights on how specific solute–solvent interactions respond to intramolecular electron transfer.[42] Additionally, in this work a fine characterization of the charged ligand carboxyl symmetric and asymmetric stretchings has been made available *via* generalized normal mode analysis. By using an accurate description of the solute–solvent interactions along with the anharmonic nature of AIMD sampling, we were able to reproduce the experimental values and link the observed shifts with respect to the gas-phase to a complex solvent distribution around ligands, mostly spherically distributed around the oxygen atoms.

Knowing the exact solvent distribution around dcbpy groups and its effect on carboxyl stretching is very important, since shifts of the order of $\sim$10 cm^{-1} can be used to distinguish between different binding motifs and detect exciton migration.[30] More broadly this work provides the grounds for future excited-state nuclear and electronic dynamics to monitor non-equilibrium processes of CT excitation in complex environments, such as exciton migration in photovoltaic applications.

Author contributions

FP, AP, and NR: project. FP: data collections. FP and AP: data analysis. All authors interpretation of data and writing.

Conflicts of interest

The are no conflicts of interest to declare.

Acknowledgements

FP and NR thanked Gaussian Inc. for financial support. Italian Ministry of Education, University and Research (MIUR) is also gratefully acknowledged for financial support (AP: Project AIM1829571-1 CUP E61G19000090002, NR: Project PRIN 2017YJMPZN001).

Published on 11 agosto 2021. Downloaded on 28/08/2024 14:03:37.

Notes and references

1 M. Grätzel, *Inorg. Chem.*, 2005, **44**, 6841–6851.
2 A. Hagfeldt, G. Boschloo, L. Sun, L. Kloo and H. Pettersson, *Chem. Rev.*, 2010, **110**, 6595–6663.
3 B. Lee, J. He, R. P. Chang and M. G. Kanatzidis, *Nature*, 2012, **485**, 486–489.
4 M. Grätzel, *J. Photochem. Photobiol., C*, 2003, **4**, 145–153.
5 M. Chergui, *Acc. Chem. Res.*, 2015, **48**, 801–808.
6 E. A. Juban, A. L. Smeigh, J. E. Monat and J. K. McCusker, *Coord. Chem. Rev.*, 2006, **250**, 1783–1791.
7 J. K. McCusker, *Acc. Chem. Res.*, 2003, **36**, 876–887.
8 M. K. Nazeeruddin, R. Humphry-Baker, P. Liska and M. Grätzel, *J. Phys. Chem. B*, 2003, **107**, 8981–8987.
9 Q.-B. Meng, K. Takahashi, X.-T. Zhang, I. Sutanto, T. Rao, O. Sato, A. Fujishima, H. Watanabe, T. Nakamori and M. Uragami, *Langmuir*, 2003, **19**, 3572–3574.
10 J. B. Asbury, R. J. Ellingson, H. N. Ghosh, S. Ferrere, A. J. Nozik and T. Lian, *J. Phys. Chem. B*, 1999, **103**, 3110–3119.
11 M. R. Waterland and D. F. Kelley, *J. Phys. Chem. A*, 2001, **105**, 4019–4028.
12 L. C. T. Shoute and G. R. Loppnow, *J. Am. Chem. Soc.*, 2003, **125**, 15636–15646.
13 B. E. Van Kuiken, N. Huse, H. Cho, M. L. Strader, M. S. Lynch, R. W. Schoenlein and M. Khalil, *J. Phys. Chem. Lett.*, 2012, **3**, 1695–1700.
14 O. Bräm, F. Messina, A. M. El-Zohry, A. Cannizzo and M. Chergui, *Chem. Phys.*, 2012, **393**, 51–57.
15 R. Horvath, M. G. Fraser, C. A. Clark, X.-Z. Sun, M. W. George and K. C. Gordon, *Inorg. Chem.*, 2015, **54**, 11697–11708.
16 Y. Tachibana, J. E. Moser, M. Grätzel, D. R. Klug and J. R. Durrant, *J. Phys. Chem.*, 1996, **100**, 20056–20062.
17 T. Hannappel, B. Burfeindt, W. Storck and F. Willig, *J. Phys. Chem. B*, 1997, **101**, 6799–6802.
18 J. R. Durrant, Y. Tachibana, I. Mercer, J. E. Moser, M. Grätzel and D. R. Klug, *Z. Phys. Chem.*, 1999, **212**, 93–98.
19 J. B. Asbury, E. Hao, Y. Wang, H. N. Ghosh and T. Lian, *J. Phys. Chem. B*, 2001, **105**, 4545–4557.
20 J. Kallioinen, G. Benkö, V. Sundström, J. E. I. Korppi-Tommola and A. P. Yartsev, *J. Phys. Chem. B*, 2002, **106**, 4396–4404.
21 J. B. Asbury, N. A. Anderson, E. Hao, X. Ai and T. Lian, *J. Phys. Chem. B*, 2003, **107**, 7376–7386.
22 N. A. Anderson and T. Lian, *Annu. Rev. Phys. Chem.*, 2005, **56**, 491–519.
23 C. C. Rich, M. A. Mattson and A. T. Krummel, *J. Phys. Chem. C*, 2016, **120**, 6601–6611.
24 J. D. Gaynor, A. Petrone, X. Li and M. Khalil, *J. Phys. Chem. Lett.*, 2018, **9**, 6289–6295.
25 J. D. Gaynor, J. Sandwisch and M. Khalil, *Nat. Chem.*, 2019, **10**, 1–9.
26 J. D. Gaynor, A. Petrone, X. Li and M. Khalil, *J. Phys. Chem. Lett.*, 2018, **9**, 6289–6295.
27 K. S. Finnie, J. R. Bartlett and J. L. Woolfrey, *Langmuir*, 1998, **14**, 2744–2749.
28 J. Tang, K. W. Kemp, S. Hoogland, K. S. Jeong, H. Liu, L. Levina, M. Furukawa, X. Wang, R. Debnath and D. Cha, *et al.*, *Nat. Mater.*, 2011, **10**, 765–771.
29 K. S. Jeong, J. Tang, H. Liu, J. Kim, A. W. Schaefer, K. Kemp, L. Levina, X. Wang, S. Hoogland, R. Debnath, L. Brzozowski, E. H. Sargent and J. B. Asbury, *ACS Nano*, 2012, **6**, 89–99.
30 J. D. Leger, M. R. Friedfeld, R. A. Beck, J. D. Gaynor, A. Petrone, X. Li, B. M. Cossairt and M. Khalil, *J. Phys. Chem. Lett.*, 2019, **10**, 1833–1839.
31 C. Adamo, M. Cossi, N. Rega and V. Barone, in *Theoretical Biochemistry*, ed. L. A. Eriksson, Theoretical and Computational Chemistry, Elsevier, Amsterdam, The Netherlands, 2001, vol. 9, pp. 467–538.
32 V. Barone, R. Improta and N. Rega, *Acc. Chem. Res.*, 2008, **41**, 605–616.
33 C. Reichardt, *Chem. Rev.*, 1994, **94**, 2319–2358.
34 E. Krystkowiak, K. Dobek and A. Maciejewski, *J. Photochem. Photobiol.*, 2006, **184**, 250–264.
35 K. M. Solntsev, D. Huppert and N. Agmon, *J. Phys. Chem. A*, 1999, **103**, 6984–6997.
36 K. M. Solntsev, D. Huppert, L. M. Tolbert and N. Agmon, *J. Am. Chem. Soc.*, 1998, **120**, 7981–7982.
37 H. A. Frank, J. A. Bautista, J. Josue, Z. Pendon, R. G. Hiller, F. P. Sharples, D. Gosztola and M. R. Wasielewski, *J. Phys. Chem. B*, 2000, **104**, 4569–4577.
38 V. Barone, N. Rega, T. Bally and G. N. Sastry, *J. Phys. Chem. A*, 1999, **103**, 217–219.
39 R. Improta, N. Rega, C. Aleman and V. Barone, *Macromolecules*, 2001, **34**, 7550–7557.
40 E. Langella, N. Rega, R. Improta, O. Crescenzi and V. Barone, *J. Comput. Chem.*, 2002, **23**, 650–661.
41 A. Petrone, G. Donati, P. Caruso and N. Rega, *J. Am. Chem. Soc.*, 2014, **136**, 14866–14874.
42 E. Biasin, Z. W. Fox, A. Andersen, K. Ledbetter, K. S. Kjær, R. Alonso-Mori, J. M. Carlstad, M. Chollet, J. D. Gaynor, J. M. Glownia, K. Hong, T. Kroll, H. J. Lee, C. Liekhus-Schmaltz, M. Reinhard, D. Sokaras, Y. Zhang, G. Doumy, A. M. March, S. H. Southworth, S. Mukamel, K. J. Gaffney, R. W. Schoenlein, N. Govind, A. A. Cordones and M. Khalil, *Nat. Chem.*, 2021, **13**, 343–349.
43 J. D. Leger, M. R. Friedfeld, R. A. Beck, J. D. Gaynor, A. Petrone, X. Li, B. M. Cossairt and M. Khalil, *J. Phys. Chem. Lett.*, 2019, **10**, 1833–1839.
44 N. Rega, *Theor. Chem. Acc.*, 2006, **116**, 347–354.
45 A. Strachan, *J. Chem. Phys.*, 2004, **120**, 1–4.
46 M.-P. Gaigeot, M. Martinez and R. Vuilleumier, *Mol. Phys.*, 2007, **105**, 2857–2878.
47 R. Beck, A. Petrone, J. M. Kasper, M. J. Crane, P. J. Pauzauskie and X. Li, *J. Phys. Chem. C*, 2018, **122**, 8573–8580.
48 A. Petrone, D. B. Williams-Young, D. B. Lingerfelt and X. Li, *J. Phys. Chem. A*, 2017, **121**, 3958–3965.
49 E. Q. Chong, D. B. Lingerfelt, A. Petrone and X. Li, *J. Phys. Chem. C*, 2016, **120**, 19434–19441.
50 J. Hafner, C. Wolverton and G. Ceder, *MRS Bull.*, 2006, **31**, 659–668.

 This journal is © the Owner Societies 2021

Published on 11 agosto 2021. Downloaded on 28/08/2024 14:03:37.

51 R. Beaulac, Y. Feng, J. W. May, E. Badaeva, D. R. Gamelin and X. Li, *Phys. Rev. B: Condens. Matter Mater. Phys.*, 2011, **84**, 195324.
52 P. J. Lestrange, P. D. Nguyen and X. Li, *J. Chem. Theory Comput.*, 2015, **11**, 2994–2999.
53 J. Aarons, M. Sarwar, D. Thompsett and C.-K. Skylaris, *J. Chem. Phys.*, 2016, **145**, 220901.
54 A. Petrone, J. J. Goings and X. Li, *Phys. Rev. B*, 2016, **94**, 165402.
55 G. Donati, D. B. Lingerfelt, A. Petrone, N. Rega and X. Li, *J. Phys. Chem. A*, 2016, **120**, 7255–7261.
56 N. Li, Z. Zhu, C.-C. Chueh, H. Liu, B. Peng, A. Petrone, X. Li, L. Wang and A. K.-Y. Jen, *Adv. Energy Mater.*, 2016, **7**, 1601307.
57 D. C. Gary, S. E. Flowers, W. Kaminsky, A. Petrone, X. Li and B. M. Cossairt, *J. Am. Chem. Soc.*, 2016, **138**, 1510–1513.
58 D. C. Gary, A. Petrone, X. Li and B. M. Cossairt, *Chem. Commun.*, 2017, **53**, 161–164.
59 J. L. Stein, M. I. Steimle, M. W. Terban, A. Petrone, S. J. L. Billinge, X. Li and B. M. Cossairt, *Chem. Mater.*, 2017, **29**, 7984–7992.
60 G. Donati, D. B. Lingerfelt, C. M. Aikens and X. Li, *J. Phys. Chem. C*, 2017, **121**, 15368–15374.
61 S. Xu, J. E. T. Smith, S. Gozem, A. I. Krylov and J. M. Weber, *Inorg. Chem.*, 2017, **56**, 7029–7037.
62 U. Raucci, M. G. Chiariello, F. Coppola, F. Perrella, M. Savarese, I. Ciofini and N. Rega, *J. Comput. Chem.*, 2020, **41**, 1835–1841.
63 E. Battista, P. L. Scognamiglio, N. Di Luise, U. Raucci, G. Donati, N. Rega, P. A. Netti and F. Causa, *J. Mater. Chem. B*, 2018, **6**, 1207–1215.
64 A. Wildman, G. Donati, F. Lipparini, B. Mennucci and X. Li, *J. Chem. Theory Comput.*, 2018, **15**, 43–51.
65 F. Perrella, U. Raucci, M. G. Chiariello, M. Chino, O. Maglio, A. Lombardi and N. Rega, *Biopolymers*, 2018, **109**, e23225.
66 G. Donati, A. Petrone, P. Caruso and N. Rega, *Chem. Sci.*, 2018, **9**, 1126–1135.
67 U. Raucci, F. Perrella, G. Donati, M. Zoppi, A. Petrone and N. Rega, *J. Comput. Chem.*, 2020, **41**, 2228–2239.
68 A. Petrone, D. B. Lingerfelt, N. Rega and X. Li, *Phys. Chem. Chem. Phys.*, 2014, **16**, 24457–24465.
69 G. Lever, D. J. Cole, R. Lonsdale, K. E. Ranaghan, D. J. Wales, A. J. Mulholland, C.-K. Skylaris and M. C. Payne, *J. Phys. Chem. Lett.*, 2014, **5**, 3614–3619.
70 A. Petrone, D. B. Lingerfelt, D. B. Williams-Young and X. Li, *J. Phys. Chem. Lett.*, 2016, **7**, 4501–4508.
71 F. Coppola, F. Perrella, A. Petrone, G. Donati and N. Rega, *Front. Mol. Biosci.*, 2020, **7**, 283.
72 R. Horvath, M. G. Fraser, C. A. Clark, X.-Z. Sun, M. W. George and K. C. Gordon, *Inorg. Chem.*, 2015, **54**, 11697–11708.
73 A. Vlček Jr and S. Záliš, *Coord. Chem. Rev.*, 2007, **251**, 258–287.
74 M. Jaeger, L. Freitag and L. Gonzalez, *Coord. Chem. Rev.*, 2015, **304**, 146–165.
75 J. E. Monat, J. H. Rodriguez and J. K. McCusker, *J. Phys. Chem. A*, 2002, **106**, 7399–7406.
76 F. De Angelis, S. Fantacci, A. Selloni, M. K. Nazeeruddin and M. Grätzel, *J. Phys. Chem. C*, 2010, **114**, 6054–6061.
77 F. De Angelis, S. Fantacci, E. Mosconi, M. K. Nazeeruddin and M. Grätzel, *J. Phys. Chem. C*, 2011, **115**, 8825–8831.
78 B. E. Van Kuiken, N. Huse, H. Cho, M. L. Strader, M. S. Lynch, R. W. Schoenlein and M. Khalil, *J. Phys. Chem. Lett.*, 2012, **3**, 1695–1700.
79 A. Y. Koposov, T. Cardolaccia, V. Albert, E. Badaeva, S. Kilina, T. J. Meyer, S. Tretiak and M. Sykora, *Langmuir*, 2011, **27**, 8377–8383.
80 T. Véry, D. Ambrosek, M. Otsuka, C. Gourlaouen, X. Assfeld, A. Monari and C. Daniel, *Chem. – Eur. J.*, 2014, **20**, 12901–12909.
81 C. Daniel, in *Absorption Spectroscopy, Emissive Properties, and Ultrafast Intersystem Crossing Processes in Transition Metal Complexes: TD-DFT and Spin–Orbit Coupling*, ed. N. Ferré, M. Filatov and M. Huix-Rotllant, Springer International Publishing, Cham, 2016, pp. 377–413.
82 T. Ono, N. Planas, P. Miró, M. Z. Ertem, E. C. Escudero-Adán, J. Benet-Buchholz, L. Gagliardi, C. J. Cramer and A. Llobet, *ChemCatChem*, 2013, **5**, 3897–3903.
83 N. Planas, T. Ono, L. Vaquer, P. Miró, J. Benet-Buchholz, L. Gagliardi, C. J. Cramer and A. Llobet, *Phys. Chem. Chem. Phys.*, 2011, **13**, 19480–19484.
84 M. Heindl, J. Hongyan, S.-A. Hua, M. Oelschlegel, F. Meyer, D. Schwarzer and L. González, *Inorg. Chem.*, 2021, **60**, 1672–1682.
85 S.-A. Hua, M. Cattaneo, M. Oelschlegel, M. Heindl, L. Schmid, S. Dechert, O. S. Wenger, I. Siewert, L. González and F. Meyer, *Inorg. Chem.*, 2020, **59**, 4972–4984.
86 M. Jäger, L. Freitag and L. González, *Coord. Chem. Rev.*, 2015, **304–305**, 146–165.
87 F. Labat, I. Ciofini, H. P. Hratchian, M. J. Frisch, K. Raghavachari and C. Adamo, *J. Phys. Chem. C*, 2011, **115**, 4297–4306.
88 I. Ciofini, C. A. Daul and C. Adamo, *J. Phys. Chem. A*, 2003, **107**, 11182–11190.
89 I. Ciofini, P. P. Lainé, F. Bedioui and C. Adamo, *J. Am. Chem. Soc.*, 2004, **126**, 10763–10777.
90 D. Case, H. Aktulga, K. Belfon, I. Ben-Shalom, S. Brozell, D. Cerutti, T. Cheatham, III, V. Cruzeiro, T. Darden, R. Duke, G. Giambasu, M. Gilson, H. Gohlke, A. Goetz, R. Harris, S. Izadi, S. Izmailov, C. Jin, K. Kasavajhala, M. Kaymak, E. King, A. Kovalenko, T. Kurtzman, T. Lee, S. LeGrand, P. Li, C. Lin, J. Liu, T. Luchko, R. Luo, M. Machado, V. Man, M. Manathunga, K. Merz, Y. Miao, O. Mikhailovskii, G. Monard, H. Nguyen, K. OHearn, A. Onufriev, F. Pan, S. Pantano, R. Qi, A. Rahnamoun, D. Roe, A. Roitberg, C. Sagui, S. Schott-Verdugo, J. Shen, C. Simmerling, N. Skrynnikov, J. Smith, J. Swails, R. Walker, J. Wang, H. Wei, R. Wolf, X. Wu, Y. Xue, D. York, S. Zhao and P. Kollman, *Amber*, 2021.
91 W. L. Jorgensen, J. Chandrasekhar, J. D. Madura, R. W. Impey and M. L. Klein, *J. Chem. Phys.*, 1983, **79**, 926–935.
92 G. Donati, A. Petrone and N. Rega, *Phys. Chem. Chem. Phys.*, 2020, **22**, 22645–22661.

Published on 11 agosto 2021. Downloaded on 28/08/2024 14:03:37.

93 A. D. Becke, *J. Chem. Phys.*, 1993, **98**, 5648.
94 C. Lee, W. Yang and R. G. Parr, *Phys. Rev. B: Condens. Matter Mater. Phys.*, 1988, **37**, 785.
95 B. Miehlich, A. Savin, H. Stoll and H. Preuss, *Chem. Phys. Lett.*, 1989, **157**, 200–206.
96 F. Weigend and R. Ahlrichs, *Phys. Chem. Chem. Phys.*, 2005, **7**, 3297–3305.
97 D. Andrae, U. Haeussermann, M. Dolg, H. Stoll and H. Preuss, *Theor. Chem. Acc.*, 1990, **77**, 123–141.
98 J. D. Gaynor, A. Petrone, X. Li and M. Khalil, *J. Phys. Chem. Lett.*, 2018, **9**, 6289–6295.
99 M. Svensson, S. Humbel, R. D. Froese, T. Matsubara, S. Sieber and K. Morokuma, *J. Phys. Chem.*, 1996, **100**, 19357–19363.
100 K. Morokuma, Q. Wang and T. Vreven, *J. Chem. Theory Comput.*, 2006, **2**, 1317–1324.
101 T. Vreven, K. S. Byun, I. Komáromi, S. Dapprich, J. A. Montgomery Jr, K. Morokuma and M. J. Frisch, *J. Chem. Theory Comput.*, 2006, **2**, 815–826.
102 L. W. Chung, W. M. C. Sameera, R. Ramozzi, A. J. Page, M. Hatanaka, G. P. Petrova, T. V. Harris, X. Li, Z. Ke, F. Liu, H.-B. Li, L. Ding and K. Morokuma, *Chem. Rev.*, 2015, **115**, 5678–5796.
103 J. Wang, R. M. Wolf, J. W. Caldwell, P. A. Kollman and D. A. Case, *J. Comput. Chem.*, 2004, **25**, 1157–1174.
104 G. Brancato, N. Rega and V. Barone, *Chem. Phys. Lett.*, 2009, **483**, 177–181.
105 N. Rega, G. Brancato and V. Barone, *Chem. Phys. Lett.*, 2006, **422**, 367–371.
106 G. Brancato, N. Rega and V. Barone, *J. Chem. Phys.*, 2008, **128**, 144501.
107 G. Brancato, V. Barone and N. Rega, *Theor. Chem. Acc.*, 2007, **117**, 1001–1015.
108 S. Miertuš, E. Scrocco and J. Tomasi, *Chem. Phys.*, 1981, **55**, 117–129.
109 B. Mennucci and J. Tomasi, *J. Chem. Phys.*, 1997, **106**, 5151–5158.
110 B. Mennucci, *Wiley Interdiscip. Rev.: Comput. Mol. Sci.*, 2012, **2**, 386–404.
111 J. Tomasi, B. Mennucci and R. Cammi, *Chem. Rev.*, 2005, **105**, 2999–3094.
112 G. Brancato, N. Rega and V. Barone, *J. Chem. Phys.*, 2008, **128**, 04B607.
113 M. Cossi, V. Barone, R. Cammi and J. Tomasi, *Chem. Phys. Lett.*, 1996, **255**, 327–335.
114 M. Cossi, G. Scalmani, N. Rega and V. Barone, *J. Chem. Phys.*, 2002, **117**, 43–54.
115 M. Cossi and V. Barone, *J. Chem. Phys.*, 2000, **112**, 2427–2435.
116 G. Brancato, A. Di Nola, V. Barone and A. Amadei, *J. Chem. Phys.*, 2005, **122**, 154109.
117 H. B. Schlegel, J. M. Millam, S. S. Iyengar, G. A. Voth, A. D. Daniels, G. E. Scuseria and M. J. Frisch, *J. Chem. Phys.*, 2001, **114**, 9758–9763.
118 S. S. Iyengar, H. B. Schlegel, J. M. Millam, G. A. Voth, G. E. Scuseria and M. J. Frisch, *J. Chem. Phys.*, 2001, **115**, 10291–10302.
119 N. Rega, S. S. Iyengar, G. A. Voth, H. B. Schlegel, T. Vreven and M. J. Frisch, *J. Phys. Chem. B*, 2004, **108**, 4210–4220.
120 M. J. Frisch, G. W. Trucks, H. B. Schlegel, G. E. Scuseria, M. A. Robb, J. R. Cheeseman, G. Scalmani, V. Barone, B. Mennucci, G. A. Petersson, H. Nakatsuji, M. Caricato, X. Li, H. P. Hratchian, A. F. Izmaylov, J. Bloino, G. Zheng, J. L. Sonnenberg, W. Liang, M. Hada, M. Ehara, K. Toyota, R. Fukuda, J. Hasegawa, M. Ishida, T. Nakajima, Y. Honda, O. Kitao, H. Nakai, T. Vreven, J. J. A. Montgomery, J. E. Peralta, F. Ogliaro, M. Bearpark, J. J. Heyd, E. Brothers, K. N. Kudin, V. N. Staroverov, T. Keith, R. Kobayashi, J. Normand, K. Raghavachari, A. Rendell, J. C. Burant, S. S. Iyengar, J. Tomasi, M. Cossi, N. Rega, J. M. Millam, M. Klene, J. E. Knox, J. B. Cross, V. Bakken, C. Adamo, J. Jaramillo, R. Gomperts, R. E. Stratmann, O. Yazyev, A. J. Austin, R. Cammi, C. Pomelli, J. W. Ochterski, R. L. Martin, K. Morokuma, V. G. Zakrzewski, G. A. Voth, P. Salvador, J. J. Dannenberg, S. Dapprich, P. V. Parandekar, N. J. Mayhall, A. D. Daniels, O. Farkas, J. B. Foresman, J. V. Ortiz, J. Cioslowski and D. J. Fox, *Gaussian Development Version Revision H.37+*, 2014.
121 S. Thicoipe, P. Carbonniere and C. Pouchan, *Chem. Phys. Lett.*, 2014, **591**, 243–247.
122 P. Carbonniere, A. Dargelos, I. Ciofini, C. Adamo and C. Pouchan, *Phys. Chem. Chem. Phys.*, 2009, **11**, 4375–4384.
123 W. Humphrey, A. Dalke and K. Schulten, *J. Mol. Graphics*, 1996, **14**, 33–38.
124 N. H. Damrauer, G. Cerullo, A. Yeh, T. R. Boussie, C. V. Shank and J. K. McCusker, *Science*, 1997, **275**, 54–57.
125 K. Kalyanasundaram, *Coord. Chem. Rev.*, 1982, **46**, 159–244.
126 A. Juris, V. Balzani, F. Barigelletti, S. Campagna, P. L. Belser and A. V. von Zelewsky, *Coord. Chem. Rev.*, 1988, **84**, 85–277.
127 E. M. Kober, B. P. Sullivan and T. J. Meyer, *Inorg. Chem.*, 1984, **23**, 2098–2104.
128 R. F. Dallinger and W. H. Woodruff, *J. Am. Chem. Soc.*, 1979, **101**, 4391–4393.
129 D. H. Oh and S. G. Boxer, *J. Am. Chem. Soc.*, 1989, **111**, 1130–1131.
130 M. Myrick, R. Blakley and M. DeArmond, *J. Am. Chem. Soc.*, 1987, **109**, 2841–2842.
131 B. P. Rimgard, J. Föhlinger, J. Petersson, M. Lundberg, B. Zietz, A. M. Woys, S. A. Miller, M. R. Wasielewski and L. Hammarström, *Chem. Sci.*, 2018, **9**, 7958–7967.
132 M. Waterland and D. Kelley, *J. Phys. Chem. A*, 2001, **105**, 4019–4028.
133 G. Benkö, J. Kallioinen, P. Myllyperkiö, F. Trif, J. E. Korppi-Tommola, A. P. Yartsev and V. Sundström, *J. Phys. Chem. B*, 2004, **108**, 2862–2867.
134 H. Zabrodsky, S. Peleg and D. Avnir, *J. Am. Chem. Soc.*, 1992, **114**, 7843–7851.
135 M. Pinsky, D. Casanova, P. Alemany, S. Alvarez, D. Avnir, C. Dryzun, Z. Kizner and A. Sterkin, *J. Comput. Chem.*, 2008, **29**, 190–197.
136 M. Pinsky, C. Dryzun, D. Casanova, P. Alemany and D. Avnir, *J. Comput. Chem.*, 2008, **29**, 2712–2721.

 This journal is © the Owner Societies 2021